



Experimental study of mechanical properties and fracture modes in different regions of the nickel-based welding joint based on small punch test

Xiangxuan Geng¹ · Jian Peng^{1,2} · Liangxiong Jiang³ · Xuedong Liu^{1,2} · Yi Tu¹ · Zhichao Xue¹

Received: 28 September 2022 / Accepted: 14 December 2022 / Published online: 26 December 2022
© International Institute of Welding 2022

Abstract

The mechanical properties and fracture mechanism in different micro-regions of the nickel-based welding joint with the ENiCrMo-3 as the electrode and 15CrMoR as the base material are studied based on small punch test (SPT) and microscopic observation. The load–displacement curves in different regions containing base metal zone (BMZ), heat-affected zone (HAZ) and welding metal zone (WMZ) are obtained by SPT, and the distribution laws of yield load P_y , the maximum load P_m , the displacement corresponding to the maximum load u_m and the fracture energy E_{SP} are analysed. The yield load P_y and the maximum load P_m in BMZ and HAZ are similar, and both are lower than those in WMZ, while the displacement corresponding to the maximum load and the fracture energy in BMZ and HAZ are similar and larger than those in WMZ. Therefore, the WMZ is with better strength, but weaker ductility than BMZ and HAZ. The fractured SPT specimens and the metallographic observations reveal that the failure mode in BMZ is the significant circular necking forming a “C” type ductile fracture. But in WMZ, the secondary cracks combined with the primary circular crack form a “Y” type fracture morphology with the mixed brittle and ductile fracture mode. In this study, the characterizations of mechanical properties and fracture modes in different micro-regions of nickel-based welding joint are achieved by SPT, which is meaningful to comprehensively understand the fracture behaviour of the nickel-based welding joint.

Keywords Nickel-based welding joint · Small punch test · Fracture mode · Micro-region · Load–displacement curve · Fracture energy

Nomenclature

P_y	Yield load (N)
P_m	Maximum load (N)
f_A	The load corresponding to point A (N)
f_B	The load corresponding to point B (N)
u_m	The displacement corresponding to the maximum load (mm)

u_A	The displacement value corresponding to point A (mm)
u_B	The displacement value corresponding to the specimen thickness (mm)
E_{SP}	Fracture energy (MJ)
E_{SPm}	The fracture energy corresponding to the maximum load of the load–displacement curve (MJ)
E_{SPw}	The fracture energy corresponding to the entire load–displacement curve (MJ)
P_{y_Mao}	Yield load derived by the method of Mao (N)
P_{y_CEN}	Yield load derived by the method in CEN (N)
P_{y_inf}	Force corresponding to the first inflexion point in SPT curves (N)
$P_{y_t/10}$	Yield load obtained by translating the tangent line of the elastic phase curve to the right by 1/10 of the thickness of the specimen t (N)
σ_y	Yield stress (MPa)
σ_{y_Mao}	Yield stress in the correlation equation proposed by Mao (MPa)

Recommended for publication by Commission X - Structural Performances of Welded Joints - Fracture Avoidance

✉ Jian Peng
joepengjian@163.com

- ¹ School of Mechanical Engineering and Rail Transit, Changzhou University, Changzhou 213164, People's Republic of China
- ² Jiangsu Province Engineering Research Center of High-Level Energy and Power Equipment, Changzhou 213164, China
- ³ Sinopec Yangzi Petrochemical Co. Ltd, Nanjing 210048, China

σ_{y_Cue}	Yield stress in the correlation equation proposed by Cue (MPa)
t	Small punch test specimen thickness (mm)
α	Empirical fitting parameter
α_1	Slope
α_2	Intercept
D	Lower die punching diameter (mm)
d	Upper die punching diameter (mm)
t_{h1}	The minimum thickness of the specimen in BMZ (mm)
t_{h2}	The minimum thickness of the specimen in WMZ (mm)
SPT	Small punch test
SMAW	Shielded metal arc welding
PWHT	Post-weld heat treatment
BMZ	Base metal zone
HAZ	Heat-affected zone
WMZ	Welding metal zone
TIG	Tungsten inert gas
A-TIG	Activating flux TIG welding
DIC	Digital image correlation

1 Introduction

Cr–Mo steel, a low carbon steel with the addition of Cr and Mo alloying elements, is with good high-temperature strength, corrosive environment resistance and oxidation resistance, widely used in pressure equipment in the severe conditions, such as oil and gas storage and processing equipment, thermal power and nuclear power equipment and steam turbine cylinder blocks [1–3]. However, the welding joint of Cr–Mo steel is usually the weak link of the equipment, and researchers paid attentions on its strength. Nagaraju et al. [4] studied the effect of shielded metal arc, tungsten inert gas (TIG) and activating flux TIG welding (A-TIG) welding processes on the microstructure evolution, mechanical properties and residual stress in different regions of 9Cr-1Mo steel welding joint, and found that the yield strength and tensile strength decreased from welding metal zone (WMZ) to base metal zone (BMZ). Storesund et al. [5] studied the effect of post-welding heat treatment on the hardness and impact toughness of 1Cr-0.5Mo and 2.25Cr-1Mo welding joint, which was performed at 720 °C with 2 h and cooled with the rate of approximately 150 °C/h. And they found that the post-weld heat treatment significantly reduced the hardness and the impact transition temperature and increased the upper shelf energy. In practical engineering applications, nickel-based electrode can be used in Cr–Mo steel welding and welding repair [6]. Bhaduri et al. [7] studied the tensile properties and impact properties of the all-weld and transverse-weld for the dissimilar metal joints of 800 alloy and 2.25Cr-1Mo steel with Inconel-182

electrodes, and analysed the effect of aging on the interfacial microstructure and mechanical properties of the welding joints. Since the nickel-based welding joint can effectively control the effect of carbon migration on the joint, Laha et al. [8] studied the mechanical properties and cracking behaviour of the similar and dissimilar joints using Inconel-182 as the welding material, and found that the creep fracture strength of the joint was lower than that of the ferritic steel base materials, with the greater strength reduction for the joint with 2.25Cr-1Mo steel as base material and the lower strength reduction for the joint with 9Cr-1Mo steel as base material. Shariatpanah [9] studied the mechanical properties and microstructure of welding joint with 316L austenitic stainless steel and 2.25Cr-1Mo steel as base materials and with Inconel-182 as the welding material. And the results showed that the average hardness, tensile plasticity and impact energy of the weld material increased with the increase of the overlay layer width, while the tensile strength properties were not significantly affected and the fracture surface of the tensile specimen showed the ductile character. The mechanical properties of Cr–Mo steel welding joints using nickel-based welding joints are of wide interest to the engineering practice. For the narrow welding zone and HAZ of Cr–Mo steel welding joints with nickel-based welding material, the traditional mechanical tests are limited by the size of the specimen and cannot obtain the local mechanical properties of each zone. Therefore, microspecimen test techniques are needed to examine the local mechanical properties of welding joint.

Small punch test (SPT) is with the advantage to understand the mechanical properties and fracture mechanics by micro-specimens [10, 11], which can be performed to study the local mechanical properties, toughness transition temperature and fracture parameters in micro-regions of the welding joint. Lyu [12] used the SPT method to study the microstructure fracture strength and ductile–brittle transition temperature of SM50YB and SM58Q steel welding joints, and found that the SPT provided a useful method to determine the reliable ductile–brittle transition temperature in various zones of steel welding joint. Nafari, M. et al. [13] found that the heat-affected zone (HAZ) is the weakest part in Incoloy 800H welding joint, and BMZ and WMZ have longer lives than HAZ. Rodríguez et al. [14] characterized the yield strength and tensile strength in the HAZ of 30CrMo5-2 welding joint using SPT, and obtained the distribution pattern of SPT strength parameters in the HAZ. Gülçimen et al. [15] characterized the mechanical property of P91 welding joint by small punch fracture tests, and found that HAZ with fine grains exhibited excellent tensile properties in terms of fracture displacement (ductility) and maximum force (strength), which is more pronounced at lower temperatures. Lee et al. [16] conducted aging treatment on the welding joints of

X20CrMoV121 steel and 2.25Cr1Mo steel to investigate the degradation of microstructure and fracture toughness in HAZ by SPT, so as to evaluate the degradation of material properties in micro-regions.

As the application of SPT expands, the SPT standard is proposed. The European Committee for Standardization released the CEN workshop agreement “Small punch Test method for metallic materials” named as CWA 15,627 in 2007 [17], which contained part A the code of practice for small punch creep testing and part B the code of practice for small punch testing for tensile and fracture behaviour. Chinese National Standard issued “Test method for small punch testing of metallic materials for in-service pressurized equipment” with GB/T 29,459 in 2012 [18], and two parts were published with part 1 general provisions and part 2 method of test for tensile properties at room temperature. The American Society for Testing and Materials issued ASTM E3205-20 “Standard Test Method for Small Punch Testing of Metallic Materials” in 2020 [19], which is under the jurisdiction of ASTM Committee E10 on Nuclear Technology and Applications. Recently, the European standard EN 10,371 “Metallic materials- Small punch test method” was approved by CEN in 2021 [20]. Standardized SPT method is the strong foundation for the application.

In order to ensure the safety and reliability in the micro-regions of nickel-based welding joints, relying on the advantages of the SPT method, the mechanical properties of the welding joint with ENiCrMo-3 as the welding material and 15CrMoR as the base material are studied focusing on the distributions of mechanical properties on BMZ, HAZ and WMZ, and through fracture analysis as well as microscopic observation, the differences of fracture mechanisms in different micro-regions of welding joint are revealed.

2 Small punch tests in different micro-regions of welding joint

The SPT system is shown in Fig. 1, which consists of mechanical property testing machine, data acquisition system and setup of SPT. Figure 1(b) shows the setup of SPT, which is consisting of upper die and lower die, and the material of setup is GH4169 high-temperature alloy. The lower die has the punching diameter of 4 mm and the 0.2 mm × 45° chamfer, and the Si₃C ceramic ball is with the diameter of 2.5 mm. The displacement loading speed is 0.1 mm/min, and the displacement is acquired by the extensometer, while the reaction force is acquired by the force sensor.

The welding joint is obtained by ENiCrMo-3 as the welding material and 15CrMoR as the base material. The 15CrMoR plates as the base material with the length of 300 mm, the width of 75 mm and the thickness of 16 mm were welded by shielded metal arc welding (SMAW). The V-shaped bevel is processed on the ledge of plate, with the bevel angle of 35° and the blunt edge of 2 mm. The SMAW welding procedure is the multi-layer multi-pass welding with the voltage of 20–25 V and current of 1–2A, which is the same as the welding procedure of skirt support and container for the coke tower in the oil refinery factory. The preheating temperature is controlled at 100 °C, and the inter-pass temperature is controlled at 100~300 °C. The welding process is carried out in strict accordance with the standard GB/T 19,867.1–2005 “Welding procedure specification for arc welding” [21]. After welding, the welding joint was inspected by X-radiological examination according to NB/T 47,013–2015 [22], and the welding joint satisfied the requirement of grade I, without obvious welding defects. The welding parameters are included in Table 1.

Fig. 1 SPT system: (a) test machine; (b) setup of SPT

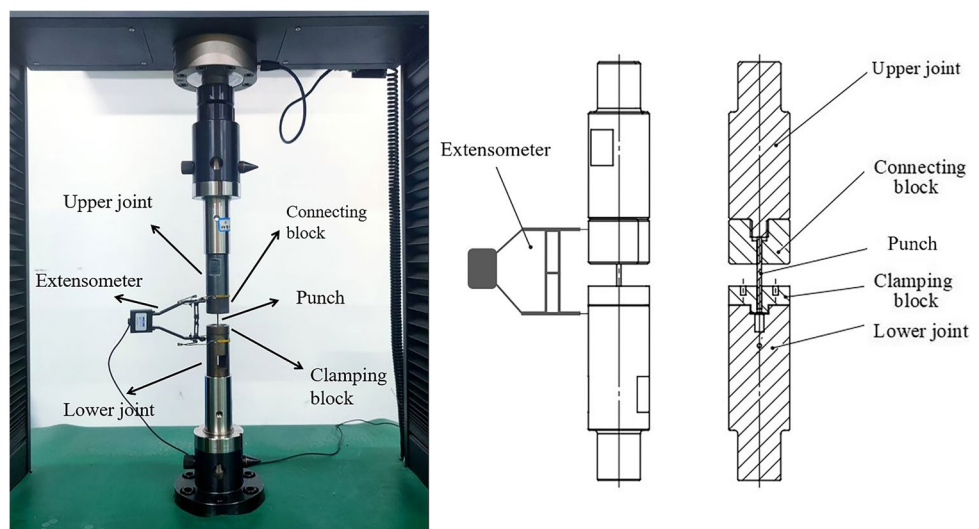
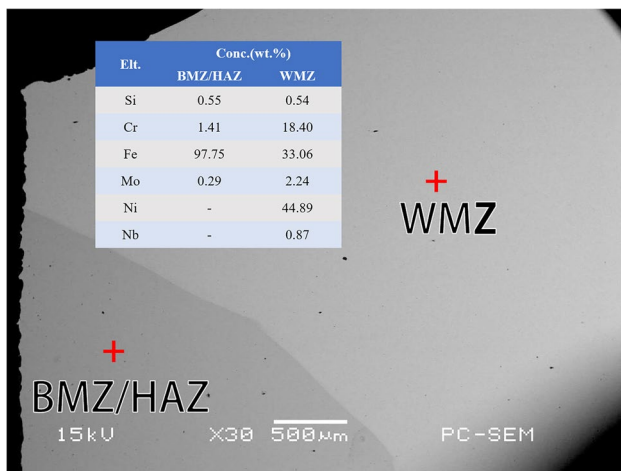


Table 1 Welding parameters and radiographic test results

Welding method	Joint type	Voltage (V)	Current (A)	Welding speed (mm·s ⁻¹)	Inspection method	Test standard	Grade
SMAW	Butt joint	20~25	120~140	1~2	Radiological examination	NB/T 47,013–2015	I

Table 2 Chemical composition of 15CrMoR base material and ENiCrMo3 weld metal (mass%)

	C	Si	Mn	Cu	Ni	Cr	Mo	Nb+Ta	Al	P	S	Fe
15CrMoR	0.08~0.18	0.15~0.4	0.4~0.7	≤0.3	≤0.3	0.8~1.2	0.45~0.6	/	/	≤0.025	≤0.01	/
ENiCrMo-3	0.1	0.5	0.5	0.5	≥58	20~23	8~10	3.15~4.15	0.4	0.02	0.15	5

**Fig. 2** Element content of each region**Table 3** Energy spectrum test results

Region	Element	keV	mass%	Error%	At%
BMZ/HAZ (15CrMoR)	Si	1.739	0.27	0.28	0.55
	Cr	5.411	1.32	0.76	1.41
	Fe	6.398	97.9	1.24	97.75
	Mo	2.293	0.51	0.75	0.29
WMZ (ENiCrMo3)	Si	1.739	0.26	0.14	0.54
	Cr	5.411	16.64	0.43	18.40
	Fe	6.398	32.11	0.59	33.06
	Ni	7.471	45.83	1.09	44.89
	Nb	2.166	1.41	0.41	0.87
	Mo	2.293	3.74	0.40	2.24

The standard chemical composition of 15CrMoR base material and ENiCrMo3 weld metal is listed in Table 2.

The actual chemical compositions on BMZ, HAZ and WMZ were obtained by the EDS energy spectrum test, and the test results are shown in Fig. 2, while the chemical compositions with the mass percentages are listed in Table 3.

The stress relief annealing post-weld heat treatment with 600 °C × 2 h + furnace cooling was used. The reason for choosing stress relief annealing heat treatment is to eliminate the effect of inhomogeneous residual stress generated during the welding process, and improve the repeatability of the experimental results.

The sampling method of the SPT micro-specimen on the welding joint is shown in Fig. 3, while the plane of SPT specimen is parallel with the fusion line to ensure the micro-structure uniformity of each SPT specimen, which can present the mechanical properties in different regions. Firstly, a round bar with the diameter of 10 mm perpendicular to the fusion line is cut by wire cutting method; then, the SPT specimen is obtained by the wire cutting method. In order to eliminate the effects caused by machining, the thickness of the cutoff discs was 0.6 mm and subsequently sandpapered to 0.5 mm.

Each micro-specimen cut from different regions was numbered and the position from the center of the welding joint was noted. Table 4 lists the thickness, distance from the fusion line, and the region where the SPT specimen belongs to, while specimens 1# to 3# are in BMZ away from the fusion line, specimens 4# to 6# are in HAZ, and specimens 7# to 12# are in WMZ. Through metallographic observation, it can be found that the coarse grain region in HAZ is less than 0.5 mm, so only the specimen with the fine grain in the HAZ is studied.

3 Results and discussion

3.1 Distribution of SPT mechanical parameters for welding joint

3.1.1 SPT load–displacement curves in different micro-regions of welding joint

The micro-specimens 1#~12# in Table 4 were tested by SPT at room temperature to obtain the load–displacement curves

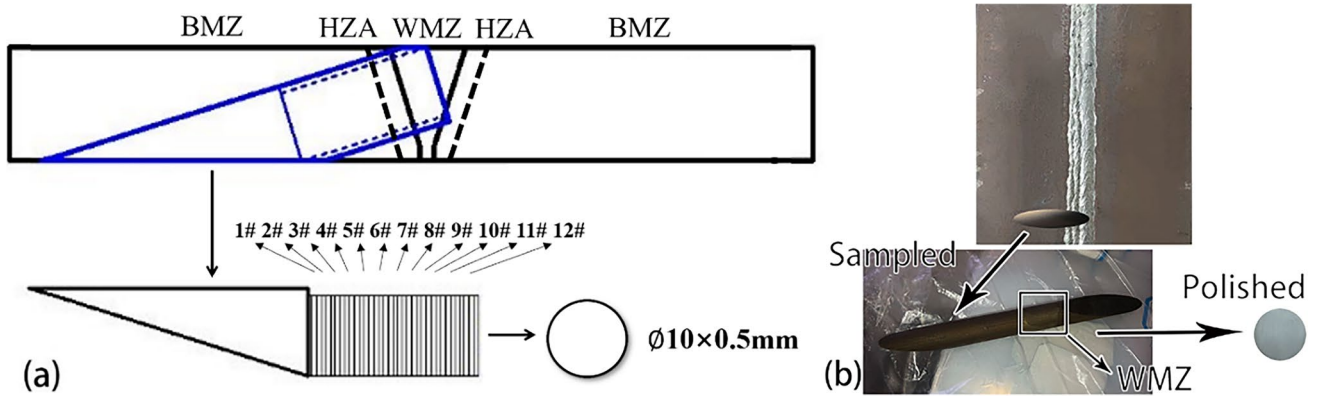


Fig. 3 Sampling of welding joint: (a) sampling method; (b) welding plate and SPT specimen

Table 4 Thickness and position of SPT specimen

Specimen number	Thickness (mm)	Distance from fusion line (mm)	Region
1#	0.502	16.8	BMZ
2#	0.500	12	BMZ
3#	0.501	7.2	BMZ
4#	0.502	2.4	HAZ
5#	0.498	1.6	HAZ
6#	0.502	0.8	HAZ
7#	0.502	-0.6	WMZ
8#	0.500	-1.2	WMZ
9#	0.500	-1.8	WMZ
10#	0.499	-2.4	WMZ
11#	0.499	-3.0	WMZ
12#	0.501	-3.6	WMZ

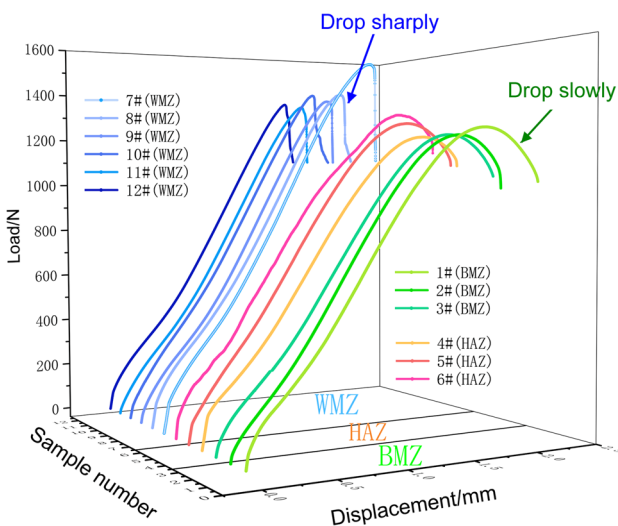


Fig. 4 Load–displacement curves in different micro-regions of welding joint

in BMZ, HAZ and WMZ for the nickel-based welding joint, as showed in Fig. 4.

In Fig. 4, the load–displacement curves in BMZ show typical ductile character, with the wide membrane stretching stage and the slowly drop stage after the maximum load is exceeded. Due to the influence of welding thermal cycle, with closer to the fusion line, the maximum load of the load–displacement curve in HAZ increases, and the slopes of elastic bending stage and plastic bending stage increase compared with those in BMZ. There is a certain variation range of the load–displacement curve in WMZ, which is related to the microstructure inhomogeneity in this zone. The differences of the membrane stretching stage and fracture damage stage among WMZ, HAZ and BMZ are obvious, in which the slope of membrane stretching stage of WMZ is highest in three zones, and in the fracture damage stage, there is a “sudden drop” phenomenon in WMZ. Moreover, the maximum load in WMZ is larger than that in BMZ and HAZ. This indicates that the strength in WMZ is higher than that in BMZ and HAZ, and there is mixed brittle and ductile failure characteristic in WMZ.

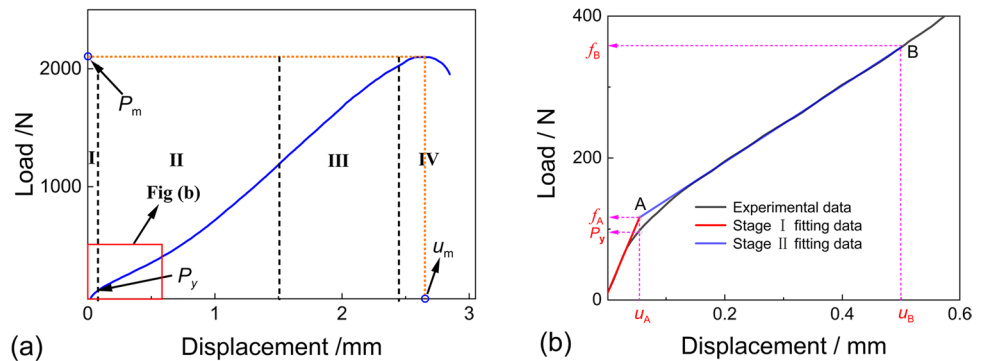
3.1.2 SPT mechanical parameters in different micro-regions of welding joint

Based on the SPT load–displacement curves in Fig. 4, the yield load P_y , the maximum load P_m , the displacement corresponding to the maximum load u_m , and the fracture energy E_{SP} are calculated as listed in Table 5. The P_m is the maximum load of the load–displacement curve, and the u_m is the horizontal axis value corresponding to the P_m . P_y is extracted by the least squares method in BS EN 10,371–2021 [20], and the determination method is shown in Fig. 5. The line segment 0-A is the linear fitting of the data in the elastic bending stage, and the line segment A-B is the linear fitting of the data in the plastic bending stage.

Table 5 SPT mechanical properties at different micro-regions

Specimen number	Zone	Yield load P_y (N)	The maximum load P_m (N)	The displacement corresponding to the maximum load u_m (mm)	Fracture energy E_{SP} (MJ)
1#	BMZ	121.99	1223.79	1.74	1231.29
2#	BMZ	115.87	1197.32	1.67	1126.21
3#	BMZ	118.96	1201.93	1.73	1166.95
4#	HAZ	128.1	1195.93	1.69	1245.41
5#	HAZ	121.5	1256.56	1.69	1335.755
6#	HAZ	133.5	1298.41	1.75	1195.548
7#	WMZ	142.16	1522.52	1.64	1350.28
8#	WMZ	136.7	1394.66	1.51	1115.01
9#	WMZ	127.81	1373.52	1.52	1062.25
10#	WMZ	127.2	1406.9	1.51	1084.41
11#	WMZ	123.68	1359.1	1.52	1036.16
12#	WMZ	132.91	1378.91	1.49	1046.96

Fig. 5 Determination of P_y : (a) SPT diagram of load–displacement curve; (b) local diagram of the yielding region of the load–displacement curve



f_A is the load corresponding to point A, where point A is the intersection of two linear fitting curves, and u_A is the displacement value corresponding to point A. f_B is the load corresponding to point B, where the value of X-axis at point B is u_B , and u_B is the displacement value corresponding to the specimen thickness. Then, the P_y is determined by the intersection point of the straight line with $x = u_A$ and the load–displacement curve.

According to the above method, the distribution patterns of strength parameters P_y and P_m in different regions were obtained, as shown in Fig. 6. It can be seen that the yield load P_y shows a fluctuating increasing trend from BMZ to WMZ, and the maximum value of P_y appears in the WMZ near the fusion line, while the minimum value appears in the BMZ. Moreover, the maximum load P_m shows almost consistent distribution law with P_y .

When the small ball punching, the SPT specimen deforms in the local zone, and with the load increasing, the specimen plastically deforms and thins. After reaching the maximum load, the cracks or voids initiate and the specimen fractures. For SPT, the plastic deformation ability of the material can be characterized by the displacement corresponding

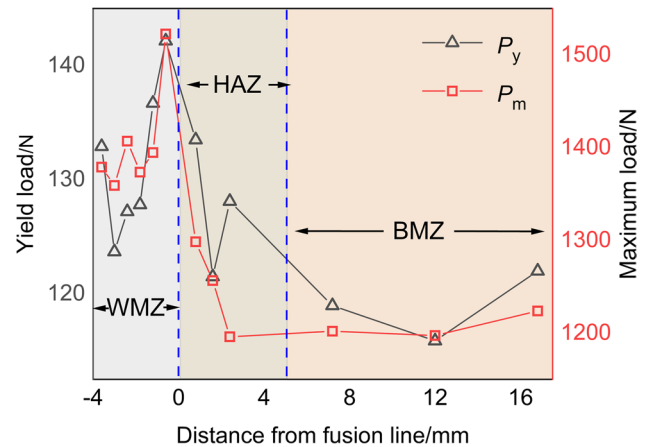


Fig. 6 Distributions of yield load and the maximum load on the welding joint

to the maximum load u_m . Fleury et al. [23] correlated the displacement corresponding to the maximum load u_m with the fracture elongation, which was a plastic parameter in the traditional tensile test, and found that the displacement

corresponding to the maximum load had a linear relationship with the fracture elongation. In order to understand the distribution of u_m on the welding joint, the distribution law of u_m in BMZ, HAZ and WMZ is shown in Fig. 7. As shown in Fig. 7, the displacement corresponding to the maximum load u_m in BMZ and HAZ is similar, but u_m in WMZ is significantly smaller than that in BMZ and HAZ, indicating that the plastic deformability in WMZ is significantly reduced, comparing with those in BMZ and HAZ.

To understand the material ductility, the fracture energy is widely used, and Fig. 8 shows the calculation method of the fracture energy of SPT.

In BS EN 10,371–2021 [20] Metallic materials–Small Punch Test method, the fracture energy E_{SPm} is considered to be the area enclosed by the load–displacement curve with the x-axis and $x = u_m$, which is corresponding to the blue area in Fig. 8. But the fracture energy of SPT is not only containing the elastic–plastic energy consumed during the specimen stable deformation period, but also the energy consumed in specimen tearing and crack propagation period. By observing the deformation process of SPT, Finarelli et al. [24] found that cracks were generated when the load reached its maximum value and cracks propagated until the load disappeared. Therefore, the energy consumed in specimen tearing and crack propagation period is also meaningful. The fracture energy E_{SPw} which is corresponding to both the blue area and red area in Fig. 8 is also used in this paper.

Figure 9 shows the fracture energy distribution in BMZ, HAZ and WMZ of the welding joint, where the fracture energy E_{SPm} is the zone enclosed by the x-axis coordinate, the load–displacement curve and the vertical line of the maximum load P_m , while the fracture energy E_{SPw} is the zone enclosed by the x-axis coordinate and the entire

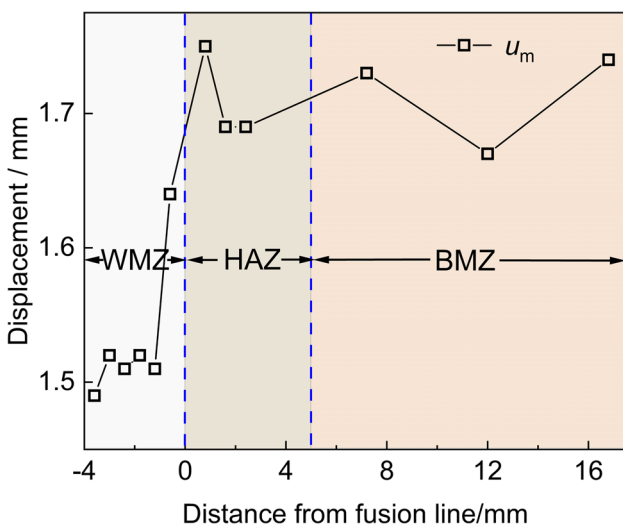


Fig. 7 Distribution of the displacement corresponding to the maximum load on the welding joint

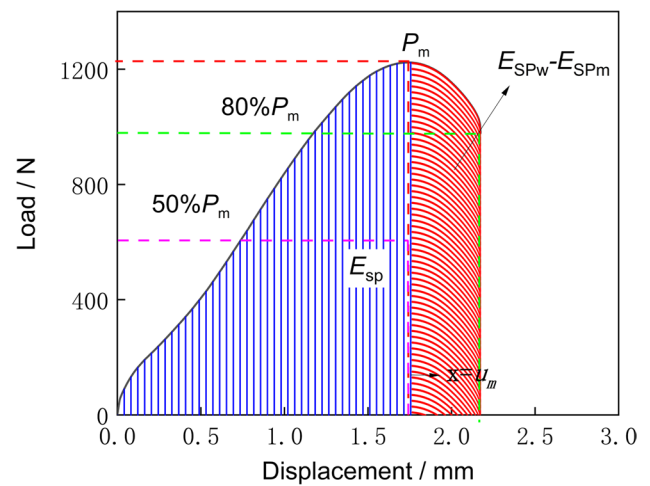


Fig. 8 Calculation of the fracture energy

load–displacement curve. It can be seen in Fig. 9 that both E_{SPm} and E_{SPw} have the similar trend, and the fracture energy in BMZ and HAZ is generally higher than that in WMZ. According to the relationship of the equivalent fracture strain and fracture toughness with the SPT fracture energy by Mao [25, 26], the fracture energy and fracture toughness are linearly correlated. Therefore, the fracture toughness in BMZ and HAZ is similar, and the fracture toughness in WMZ is lower than that in BMZ and HAZ for the nickel-based welding joint.

3.1.3 Correlation between SPT yield load and yield stress in different micro-regions of welding joint

To estimate the tensile test yield stress by the SPT yield load, Mao et al. [27] proposed correlation Eq. (1):

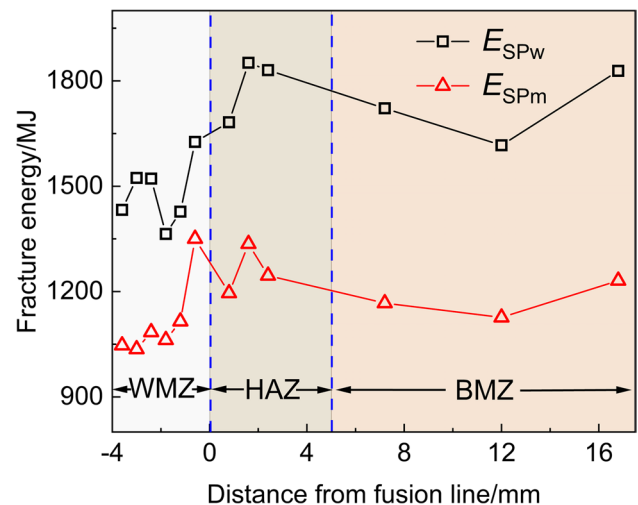


Fig. 9 Distribution of fracture energy on the welding joint

$$\sigma_{y_Mao} = \alpha \cdot \frac{P_y}{t^2} \quad (1)$$

where σ_y is the yield stress of the material, P_y is the SPT yield load and t is the SPT specimen thickness. α is the empirical fitting parameter. Table 6 lists the parameter α obtained by different researchers [28–30] for different materials, and it can be seen that the parameter α varies from 0.343 to 0.476, indicating that the value of the parameter α is depending on the material. Moreover, Leclerc Nicolas et al. [31] studied the correlation between the load–displacement curve and the tensile stress–strain curve, and pointed out that the parameter α was also depending on the determining method of the yield load and the dimensions of the SPT setup.

Cuesta et al. [32, 33] proposed a more suitable correlation Eq. (2) to correlate σ_y and P_y :

$$\sigma_{y_Mao} = \alpha_1 \cdot \frac{P_y}{t^2} + \alpha_2 \quad (2)$$

The researchers [32, 34–38] employed Eq. (2) to correlate σ_y and P_y , and some of the values of α_1 and α_2 are listed in Table 7, which also indicates the value of the parameters α_1 and α_2 is depending on the material, especially the parameter α_2 .

In order to correlate the SPT mechanical parameters with the material mechanical properties in different micro-regions of the welding joint, the digital image correlation (DIC)

technique is used to capture the local mechanical properties on the welding joint [39, 40], and the local mechanical property parameters in the SPT sampling location can be determined.

As showed in Fig. 10(a), with the DIC strain measurements, the strain map was captured in the small punch sampling zone of the welding joint. Then, the stress–strain curves in different positions were constructed by strain map and load data in Fig. 10(b). In Fig. 10(c), the yield stress was obtained from the stress–strain curve and the distribution of the yield stress on the welding joint was plotted. Since during the tensile test the welding joint fractures in BMZ, the entire stress–strain curve can be obtained by the DIC method in BMZ, but only part of plastic stage of stress–strain curve can be obtained in HAZ and WMZ. And the distribution of the ultimate strength in different regions cannot be obtained by DIC. Therefore, only the SPT yield load is correlated with the DIC yield stress in this paper.

The DIC yield stress and SPT yield load are plotted in Fig. 11. The data in BMZ and HAZ have the similar relation, but the data in WMZ is different with those in BMZ and HAZ. Therefore, the correlation equations are fitting for two groups, and the correlation Eq. (1) and Eq. (2) are compared. The DIC yield stress and SPT yield load in BMZ and HAZ are fitted based on Eq. (1) and Eq. (2) as follows:

$$\sigma_{y_Mao} = 0.821 \cdot \frac{P_y}{t^2} \quad (3)$$

Table 6 Constants α of different metals

α	Material	The method of determining P_y	Lower die D (mm)	Upper die d (mm)	References
0.360	Ferritic alloys with Cu, P, and/or C alloying elements	P_{y_Mao}	4	2.5	[28]
0.380	HAZ of 30CrMo5-2	$P_{y_l/10}$	4	2.5	[14]
0.442	Steel and aluminum alloy	P_{y_Mao}	4	2.4	[14]
0.476	Steel and aluminum alloy	P_{y_CEN}	4	2.4	[30]
0.364	Steel and aluminum alloy	$P_{y_l/10}$	4	2.4	[30]
0.343	Sintered Mo pre-alloyed and diffusion-alloyed	$P_{y_l/10}$	4	2.5	[29]

Table 7 Constants α_1 and α_2 for different metals

α_1	α_2	Material	The method of determining P_y	Lower die D (mm)	Upper die d (mm)	References
0.3	61	HAZ of low-activation ferritic steels	P_{y_Mao}	-	≈ 1	[36]
0.34~0.48	41~257	Martensitic steel EUROFER97	P_{y_CEN}	-	1	[38]
0.892	-161.9	Aluminum alloy	P_{y_Mao}	4	2.5	[32]
0.268	207	Structural steel AE460	$P_{y_l/10}$	4	2.5	[34]
0.535	14	Cr–Mo steel	$P_{y_l/10}$	4	2.5	[37]
0.633	12.4	Cr–Mo steel	P_{y_inf}	4	2.5	[37]

Fig. 10 Determination of yield stress by DIC on the welding joint: (a) strain map by DIC; (b) stress–strain curve by DIC; (c) yield stress distribution

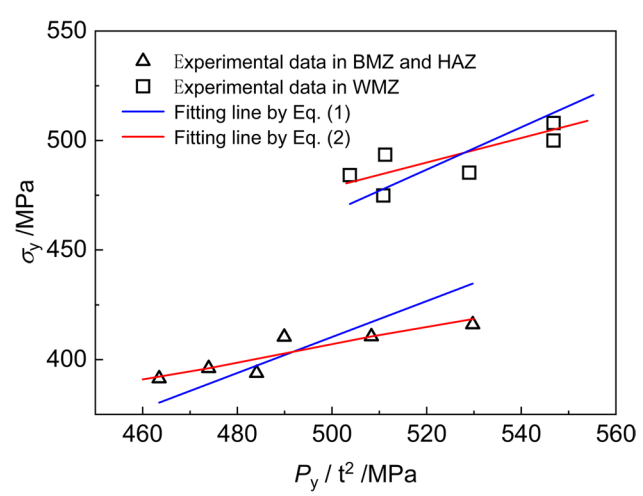
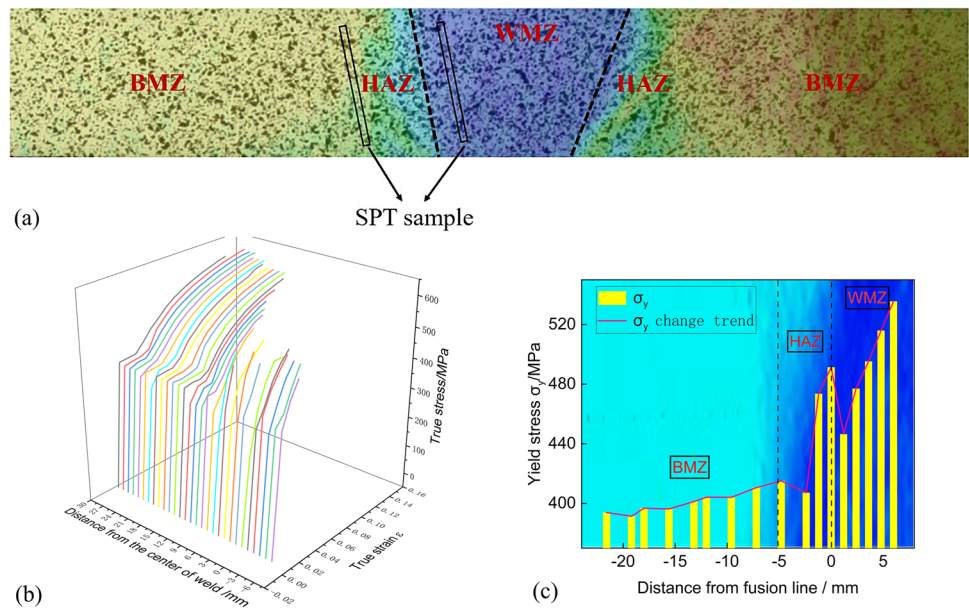


Fig. 11 Correlation of SPT P_y/t^2 and σ_y on the welding joint

$$\sigma_{y_Cue} = 0.388 \cdot \frac{P_y}{t^2} + 213.32 \tag{4}$$

The yield stress and SPT yield load in WMZ are fitted based on Eq. (1) and Eq. (2) as follows:

$$\sigma_{y_Mao} = 0.935 \cdot \frac{P_y}{t^2} \tag{5}$$

$$\sigma_{y_Cue} = 0.519 \cdot \frac{P_y}{t^2} + 219.373 \tag{6}$$

The yield stress at different micro-regions is estimated by the SPT yield loads according to the correlation equations, and the predicted data are compared with the DIC

data in Fig. 12. As shown in Fig. 12(a), the predicted yield stress can well describe the distribution of yield stress on the welding joint, and as shown in Fig. 12(b), Eq. (2) is with narrower scatter interval. Therefore, based on the correlation equations with two separate groups, the yield stress estimated by SPT yield load is in good agreement with the DIC test data.

3.2 Failure mode and damage analysis in different micro-regions of welding joint

3.2.1 Failure mode in different micro-regions of welding joint

For SPT, three types of failure modes can be classified from ductile to brittle by combining the macroscopic characteristics of SPT fractured specimen [16, 41]: (1) the first is the ductility failure mode, where the specimen undergoes significant plastic deformation, necking appears before fracture and the circular necking region is the path of the main crack propagation, forming a “C” type crack; (2) the second is a mixed ductility-brittle failure mode, i.e. the specimen undergoes a limited amount of necking deformation before fracture, and the main crack propagates in both the circular and radial directions, forming a “Y” or “T” type crack; (3) the third is the brittle failure mode, where the specimen undergoes almost no necking deformation before fracture. The fractured specimen is almost no thinning, and the main crack initiates from the center to the radial direction, forming a “X” type crack.

Figure 13 shows the fracture morphology of SPT specimen in different micro-regions of the nickel-based welding joint studied in this paper. The “cup-shaped bulge” can

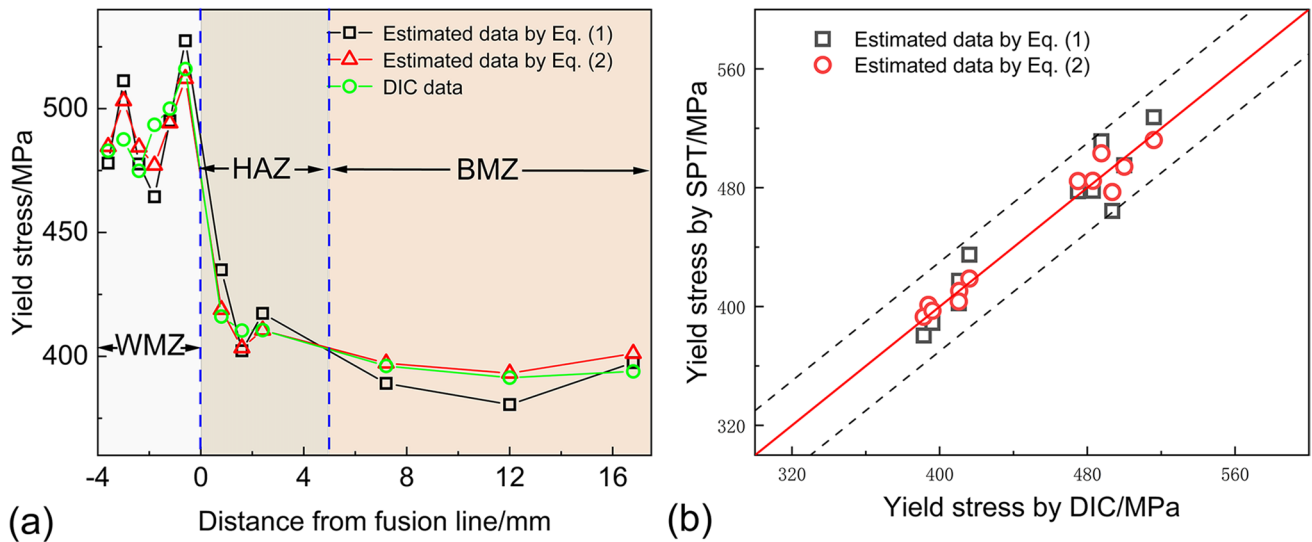
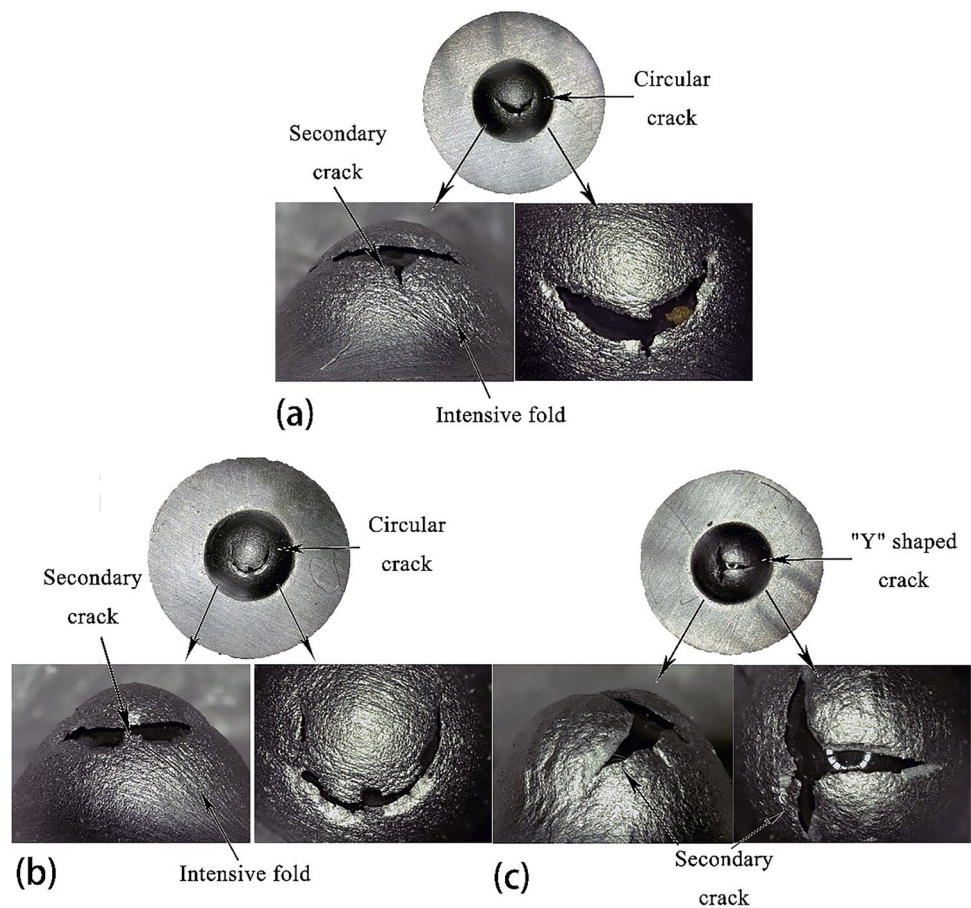


Fig. 12 Comparison of SPT predicted values with DIC measured values: (a) from the view of distribution; (b) from the view of value

Fig. 13 Fracture morphology of SPT fractured specimen in different micro-regions: (a) BMZ; (b) HAZ; (c) WMZ



be observed in the fractured specimen of BMZ and HAZ in Fig. 13(a) and (b), and the deep and dense folds appear on the surfaces of deformation zones, which is caused by the large plastic deformation during the test. Due to the

significant necking phenomenon in the plastic deformed region, the main crack in the circular direction is generated forming a "C" style crack and there are very small secondary radial cracks combined with the main circular crack, which

indicates that the failure mode in BMZ and HAZ is ductility failure dominated by plastic deformation. The fracture morphology of the micro-specimen in the WMZ is shown in Fig. 13(c). The folds on the deformed surface are sparse and inhomogeneous, and there is rarely circular necking in the fractured zone. It should be noted that the primary crack and secondary crack form a “Y” type crack on the fracture morphology. Therefore, the failure mode in WMZ is a mixed ductility-brittle failure mode and dominated by brittleness.

The analyses of fracture morphology prove that the fracture mechanisms in BMZ and HAZ are similar with the ductile fracture mode caused by the large plastic deformation in the circular direction, while the fracture mechanism in WMZ is the brittle dominated mixed fracture mode caused by the crack propagation in both circular and radial directions. The fracture mechanisms in BMZ, HAZ and WMZ indicate that the plastic deformability in WMZ is weaker than that in BMZ and HAZ.

3.2.2 Microstructure damage analysis in different micro-regions of welding joint

In order to understand the differences of microstructure damage in different micro-regions of nickel-based welding joint, the metallographic microstructures on cross-sections of fractured specimens in BMZ and WMZ are observed in Fig. 14. Since the failure modes in BMZ and HAZ are similar, only the microstructures in BMZ are given. Firstly, the fractured SPT specimens were inlaid by polyester and cut in the direction of the dashed lines shown in Fig. 14(a) and (b). They were sequentially grinded with 800#–2000# metallographic sandpaper, then polished to remove surface scratches, and washed with ethanol. In order to observe the microstructure of the fractured section, the specimens of BMZ and WMZ were etched with nitric acid and an aqua regia solution mixed with hydrochloric acid (HCl) and nitric acid (HNO₃) in the volume ratio of 3:1, respectively.

Figure 14(a-base) shows the cross-section characteristics of the fractured SPT specimen in BMZ. It can be seen that the necking thinning phenomenon is very obvious near the circular crack, in which the minimum thickness t_{h1} is 0.18 mm and the thickness thinning ratio is about 64%, so the failure mode is ductile failure caused by large deformation. Figure 14(b-weld) shows the cross-section characteristics of the fractured SPT specimen in WMZ. Opposition to the characteristics in BMZ, the cross-section in WMZ shows the un-necking characteristic even in the cracked zone, and with the minimum thickness t_{h2} of 0.33 mm and the thickness reduction ratio of 34%. Therefore, the difference of the necking phenomenon between BMZ and WMZ is clearly captured in the cross-section observation.

Figures 14(A₁)~(C₁) give the enlarged views of local zones A₁~C₁ in Fig. 14(a-base) of BMZ, where A₁ is the

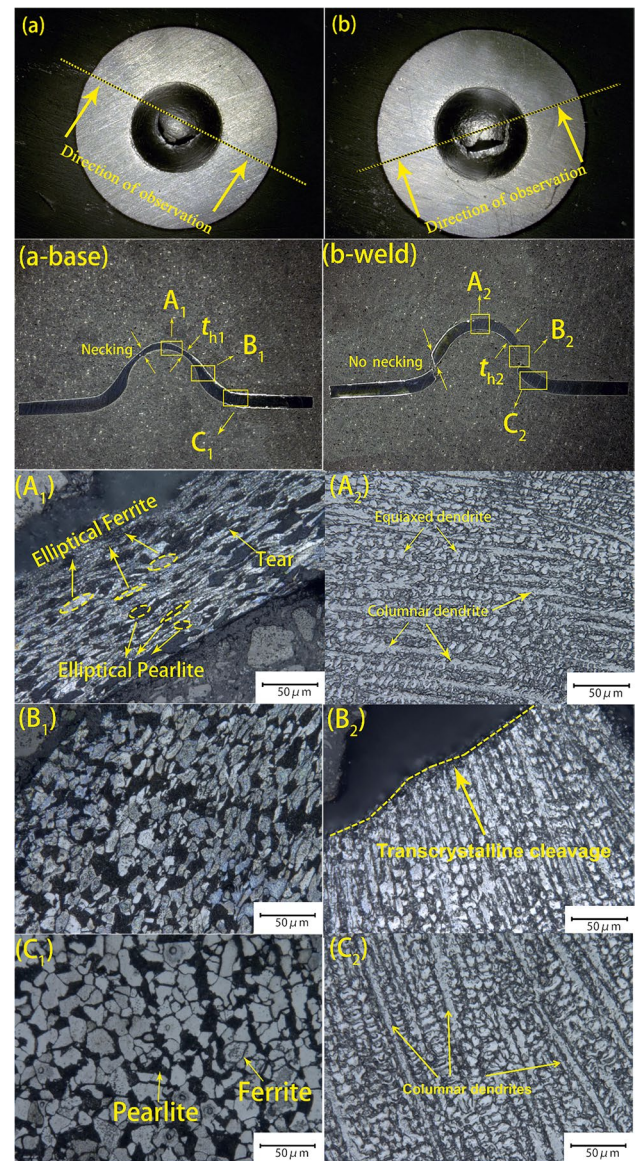


Fig. 14 Metallographic microstructure of fractured SPT specimen in BMZ (left) and WMZ (right): (a) cutting line of BMZ; (b) cutting line of WMZ; (a-base) the overall view in BMZ; (b-weld) the overall view in WMZ; (A₁), (B₁), (C₁) magnified zones in BMZ; (A₂), (B₂), (C₂) magnified zones in WMZ

central zone of the specimen, B₁ is the membrane stretching zone near failure and C₁ is the bending deformation zone. The microstructure observations in BMZ compose of pearlite and ferrite, where the brighter colour is ferrite and the darker one is pearlite. As shown in Fig. 14(A₁) of the severely plastic deformed zone, most of the ferrite grains are elongated from ball shape to elliptical shape, and part of ferrite grains are teared. The grain size of B₁ near the failure zone in Fig. 14(B₁) is smaller than that in the bending deformation zone C₁ in Fig. 14(C₁), which is due to the grain refinement caused by the large plastic deformation in B₁ near

the failure zone. During the plastic deformation of metallic materials, the dislocations at the grain boundaries and within the grain are activated resulting to the slip movement. Hughes et al. [42] found that the grain refinement during severely plastic deformation was the result of the dislocation slip. In BMZ, due to the tensile deformation of ferrite and pearlite by the external force, the ferrite cannot get rid of the surrounding pearlite and the bondage of grain boundary, resulting in the distortion deformation of ferrite grains. In addition, the deformation ability of pearlite is weaker than that of ferrite, leading to the appearances of voids and micro-cracks between ferrite grain and pearlite grain [43]. As the plastic deformation increases, the voids preferentially nucleate along the slip zone, and when the voids grow to a certain size, micro-cracks appear [44]. With the loading increasing, the cracks propagate along the severely deformed ferrite and pearlite grains, and finally, the specimen is ductile fractured.

Figures 14(A₂)~(C₂) show the enlarged views of local zones A₂~C₂ in Fig. 14 (b-weld) of WMZ, where A₂ is the central zone of the specimen, B₂ is the fracture zone and C₂ is the bending deformation zone. As shown in Fig. 14(A₂) and (C₂), mixed equiaxed and long dendrite can be observed in WMZ. The columnar dendrites in the intermediate channels are predominant, and the discontinuous equiaxed dendrites in the columnar structure of the fusion zone can also be observed. In Fig. 14(B₂), for the fracture microstructure zone B₂, fine dendrite fragments are observed at the fracture location, and the fracture extends along the direction approximately perpendicular to the dendrite stem, which is due to the bending of the primary dendrite during the deformation of the SPT specimen. Once the stress value exceeded the fracture strength, the primary dendrites brittlely fracture. In the WMZ, when the primary dendrite is perpendicular to the loading direction, the crack may propagate along the direction with lower dendrite bond strength, while when the primary dendrite is parallel to the loading direction, it may induce transcrystalline fracture, and the cleavage morphology appears on the fracture path of dendrite. Since the loading direction for the SPT specimen is closer to parallel to the primary dendrite, and the plastic deformation at fracture section is limited, the failure mode of the SPT micro-specimen in WMZ is the mixture cleavage brittle and ductile fracture.

4 Conclusions

In this paper, the mechanical properties and fracture mechanism in different micro-regions of the nickel-based welding joint are studied by SPT. Conclusions are as follows:

- (1) SPT strength parameters, containing yield load and the maximum load, increase from BMZ to WMZ, and there is some dispersion in WMZ. Based on the yield stress

obtained by the DIC test, correlation equations of yield load and yield stress are constructed for BMZ, HAZ and WMZ separately.

- (2) The displacement corresponding to the maximum load u_m in BMZ and HAZ is similar, and greater than that in WMZ, while the SPT fracture energy in BMZ and HAZ is generally higher than that in WMZ. BMZ and HAZ have similar plastic deformability and fracture toughness, and the plasticity and toughness parameters in WMZ are lower than those in BMZ and HAZ.
- (3) The fracture mode in BMZ and HAZ is with the “C” type fracture morphology, and the necking phenomenon is obvious around the fracture section, which is a typical ductile fracture due to the massive plastic deformation resulting in the creation of holes between pearlite phase and ferrite phase. The fracture mode in WMZ is with the “Y” type fracture morphology, that is the secondary cracks combined with the primary crack, and the circular necking is inapparent, which is a mixture brittle and ductile fracture mode.

Funding This work received supports from the National Natural Science Foundation of China, grant number 52075050; Natural Science Foundation of Jiangsu Province, grant number BK20201448; and Post-graduate Research & Practice Innovation Program of Jiangsu Province, grant number, SJCX22_1427.

Data Availability The data underlying this article will be shared on reasonable request to the corresponding author.

Declarations

Conflict of interest The authors declare no competing interests.

References

1. Shimazu H, Konosu S, Tanaka Y, Yuga M, Yamamoto H, Ohtsuka N (2013) Combined effect of temper and hydrogen embrittlement on threshold for hydrogen-induced fracture in cr-mo steels. *J Press Vessel Technol* 135(2):021406. <https://doi.org/10.1115/1.4023423>
2. Yu X (2014) Correlation of ferrite formation to creep properties of Cr-Mo steel welds. *Weld World* 59(2):251–259. <https://doi.org/10.1007/s40194-014-0200-5>
3. Albert SK, Ramasubbu V, Sundar Raj SI, Bhaduri AA (2013) Hydrogen-Assisted Cracking Susceptibility of modified 9Cr-1 Mo steel and its weld metal. *Weld World* 55(7–8):66–74. <https://doi.org/10.1007/bf03321309>
4. Nagaraju S, Vasantharaja P, Brahadees G, Vasudevan M, Mahadevan S (2017) Effect of Welding Processes on the Microstructure, Mechanical Properties and Residual Stresses of Plain 9Cr-1Mo Steel Weld Joints. *J Mater Eng Perform* 26(12):5938–5953. <https://doi.org/10.1007/s11665-017-3077-9>
5. Storesund J, Sandström R (1995) Influence of post weld heat treatment on impact toughness properties of 1Cr0.5Mo and

- 2.25Cr1Mo steels. *Steel Res* 66(3):117–123. <https://doi.org/10.1002/srin.199501099>
6. Sireesha M, Albert SK, Sundaresan S (2001) Microstructure and Mechanical Properties of Weld Fusion Zones in Modified 9Cr-1Mo Steel. *J Mater Eng Perform* 10(3):320–330. <https://doi.org/10.1361/105994901770345033>
 7. Bhaduri AK, Seetharaman V, Venkadesan S (1989) Effect of ageing on the interfacial microstructure and mechanical properties of an alloy 800/2.25 Cr-1 Mo steel joint. *Int J Mater Res* 80(9):630–634. <https://doi.org/10.1515/ijmr-1989-800905>
 8. Laha K, Chandravathi KS, Parameswaran P, Goyal S, Mathew MD (2011) A Comparison of Creep Rupture Strength of Ferritic/Austenitic Dissimilar Weld Joints of Different Grades of Cr-Mo Ferritic Steels. *Metall and Mater Trans A* 43(4):1174–1186. <https://doi.org/10.1007/s11661-011-0957-8>
 9. Shariatpanahi AM, Farhangi H (2009) Microstructure and Mechanical Properties of Dissimilar Ferritic and Austenitic Steel Joints with an Intermediate Inconel-182 Buttering Layer. *Adv Mater Res* 83–86:449–456. <https://doi.org/10.4028/www.scientific.net/AMR.83-86.449>
 10. Yang S, Xue L, Lu W, Ling X (2020) Experimental study on the mechanical strength and dynamic strain aging of Inconel 617 using small punch test. *J Alloy Compd* 815:152447. <https://doi.org/10.1016/j.jallcom.2019.152447>
 11. Mandziej ST, Vyrostkova A, Solar M (2013) Evolution Of Cr-Mo-Vweld Metal Microstructure during creep testing Part 2: P24 material. *Weld World* 55(5–6):52–69. <https://doi.org/10.1007/bf03321295>
 12. Lyu DY, You HS, Jung HD, Lim JK, Chung SH (1991) Fracture Strength Evaluation of Welded Joint in Steels by Using Small Punch Test. *Key Eng Mater* 51–52:435–440. <https://doi.org/10.4028/www.scientific.net/KEM.51-52.435>
 13. Nafari M, Salemi Golezani A (2018) Heat affected zone creep characterization of INCOLOY 800H by means of small punch test. *Eng Fail Anal* 94:407–411. <https://doi.org/10.1016/j.engfailanal.2018.08.020>
 14. Rodríguez C, Cabezas JG, Cárdenas E, Belzunce FJ, Journal CBJW (2009) Mechanical properties characterization of heat-affected zone using the small punch test. *Weld J* 88(9):188–192
 15. Gülçimen B, Durmuş A, Ülkü S, Hurst RC, Turba K, Hähner P (2013) Mechanical characterisation of a P91 weldment by means of small punch fracture testing. *Int J Press Vessels Pip* 105–106:28–35. <https://doi.org/10.1016/j.ijpvp.2013.02.005>
 16. Lee D-H, Kim H-S (2008) A Study on the Correlation between Advanced Small Punch Test and Charpy V-notch Test on X20CrMoV121 and 2.25Cr1Mo steels Weldment. *J Korean Weld Join Soci* 26(3):37–44. <https://doi.org/10.5781/kwjs.2008.26.3.037>
 17. CWA 15627 (2007) Small punch test method for metallic material. European Committee for Standardization, Brussels, Belgium
 18. GB/T 29459 (2012) Test method for small punch testing of metallic materials for in-service pressurized equipment. China National Standardization Management Committee, Beijing, China
 19. ASTM E3205 (2020) Standard test method for small punch testing of metallic materials. ASTM International, Pennsylvania, United States
 20. BS EN 10371 (2021) Metallic materials- Small punch test method. British Standards Institution, London, UK
 21. GB/T 19867.1 (2005) Welding procedure specification for arc welding. China National Standardization Management Committee, Beijing, China
 22. NB/T 47013-2015 (2015) Non-destructive testing of pressure equipments. China National Standardization Management Committee, Beijing, China
 23. Ha JS, Fleury E (1998) Small punch tests to estimate the mechanical properties of steels for steam power plant: II. Fracture toughness. *Int J Press Vessel Pip* 75(9):707–713. [https://doi.org/10.1016/s0308-0161\(98\)00075-1](https://doi.org/10.1016/s0308-0161(98)00075-1)
 24. Finarelli D, Carsughi F, Jung P (2008) The small ball punch test at FZJ. *J Nucl Mater* 377(1):65–71. <https://doi.org/10.1016/j.jnucmat.2008.02.053>
 25. Mao X, Saito M, Takahashi H (1991) Small punch test to predict ductile fracture toughness JIC and brittle fracture toughness KIC. *Scr Metall Mater* 25(11):2481–2485. [https://doi.org/10.1016/0956-716x\(91\)90053-4](https://doi.org/10.1016/0956-716x(91)90053-4)
 26. Mao X, Takahashi H, Kodaira T (1992) Use of Sub-sized Specimen for Evaluating the Strength and Fracture Toughness of Irradiated 2 1/4 Cr-1 MO Steel. *J Eng Mater Technol* 114(2):168–171. <https://doi.org/10.1115/1.2904157>
 27. Mao X, Takahashi H (1987) Development of a further-miniaturized specimen of 3 mm diameter for tem disk (ϕ 3 mm) small punch tests. *J Nucl Mater* 150(1):42–52. [https://doi.org/10.1016/0022-3115\(87\)90092-4](https://doi.org/10.1016/0022-3115(87)90092-4)
 28. Mao X, Kameda J (1991) Small-punch technique for measurement of material degradation of irradiated ferritic alloys. *J Mater Sci* 26(9):2436–2440. <https://doi.org/10.1007/bf01130192>
 29. Rodríguez C, Fernández M, Cabezas JG, García TE, Belzunce FJ (2016) The use of the small punch test to solve practical engineering problems. *Theoret Appl Fract Mech* 86:109–116. <https://doi.org/10.1016/j.tafmec.2016.08.021>
 30. García TE, Rodríguez C, Belzunce FJ, Suárez C (2014) Estimation of the mechanical properties of metallic materials by means of the small punch test. *J Alloy Compd* 582:708–717. <https://doi.org/10.1016/j.jallcom.2013.08.009>
 31. Leclerc N, Khosravani A, Hashemi S, Miracle DB, Kalidindi SR (2021) Correlation of measured load-displacement curves in small punch tests with tensile stress-strain curves. *Acta Mater* 204:116501. <https://doi.org/10.1016/j.actamat.2020.116501>
 32. Cuesta II, Alegre JM (2012) Hardening evaluation of stamped aluminium alloy components using the Small Punch Test. *Eng Fail Anal* 26:240–246. <https://doi.org/10.1016/j.engfailanal.2012.06.004>
 33. Álvarez G, Zafra A, Rodríguez C, Belzunce FJ, Cuesta II (2020) SPT analysis of hydrogen embrittlement in CrMoV welds. *Theoret Appl Fract Mech* 110:102813. <https://doi.org/10.1016/j.tafmec.2020.102813>
 34. Contreras MA, Rodríguez C, Belzunce FJ, BetegÓN C (2008) Use of the small punch test to determine the ductile-to-brittle transition temperature of structural steels. *Fatigue Fract Eng Mater Struct* 31(9):727–737. <https://doi.org/10.1111/j.1460-2695.2008.01259.x>
 35. Dorazil O, Matocha K, Zhu J, Chen Y (2016) The effect of long term exposition at 540 °C on the empirical correlations for determination of mechanical properties of low alloy CrMoV steel from the results of Small Punch tests. *Perspect Sci* 7:156–160. <https://doi.org/10.1016/j.pisc.2015.11.025>
 36. Kato T, Komazaki S-I, Kohno Y, Tanigawa H, Kohyama A (2009) High-temperature strength analysis of welded joint of RAFs by small punch test. *J Nucl Mater* 386–388:520–524. <https://doi.org/10.1016/j.jnucmat.2008.12.153>
 37. Singh SP, Bhattacharya S, Sehgal DK (2014) Evaluation of e mechanical strength of Cr–Mo grade steel through small punch test technique. *Eng Fail Anal* 39:207–220. <https://doi.org/10.1016/j.engfailanal.2014.01.014>
 38. Ruan Y, Spätig P, Victoria M (2002) Assessment of mechanical properties of the martensitic steel EUROFER97 by means of punch tests. *J Nucl Mater* 307–311:236–239. [https://doi.org/10.1016/s0022-3115\(02\)01194-7](https://doi.org/10.1016/s0022-3115(02)01194-7)
 39. Xie X-F, Li J, Jiang W, Dong Z, Tu S-T, Zhai X, Zhao X (2020) Nonhomogeneous microstructure formation and its role on tensile and fatigue performance of duplex stainless steel 2205 multipass weld joints. *Mater Sci Eng: A* 786:139426. <https://doi.org/10.1016/j.msea.2020.139426>

40. Sriba A, Bouquerel J, Vogt J-B (2022) DIC-aided analysis of the fatigue behaviour of a welded 316L stainless steel. *Weld World* 66(9):1915–1927. <https://doi.org/10.1007/s40194-022-01355-9>
41. Mandziej ST, Vrostkova A, Chovet C (2013) Microstructure and Creep Rupture of P92-grade weld metal. *Weld World* 55(5–6):37–51. <https://doi.org/10.1007/bf03321294>
42. Hughes DA, Hansen N (1997) High angle boundaries formed by grain subdivision mechanisms. *Acta Mater* 45(9):3871–3886. [https://doi.org/10.1016/s1359-6454\(97\)00027-x](https://doi.org/10.1016/s1359-6454(97)00027-x)
43. Schönmaier H, Grimm F, Krein R, Kirchheimer K, Schnitzer R (2019) Microstructural evolution of 2.25Cr-1Mo-0.25V submerged-arc weld metal. *Weld World* 64(2):379–393. <https://doi.org/10.1007/s40194-019-00839-5>
44. Zhang Y-C, Jiang W, Tu S-T, Zhang X-C (2022) Fracture toughness assessment of the X80 steel by nanoindentation technique and a modified constitutive model. *Theoret Appl Fract Mech* 117:103195. <https://doi.org/10.1016/j.tafmec.2021.103195>

Publisher's note Springer Nature remains neutral with regard to jurisdictional claims in published maps and institutional affiliations.

Springer Nature or its licensor (e.g. a society or other partner) holds exclusive rights to this article under a publishing agreement with the author(s) or other rightsholder(s); author self-archiving of the accepted manuscript version of this article is solely governed by the terms of such publishing agreement and applicable law.